

## Supporting Information

### Activation of C-H bonds by a nonheme iron(IV)-oxo complex: mechanistic evidence through a coupled EDXAS/UV-Vis multivariate analysis

Francesco Tavani,<sup>a,\*</sup> Giorgio Capocasa,<sup>a</sup> Andrea Martini,<sup>b,c</sup>  
Francesco Sessa,<sup>a</sup> Stefano Di Stefano,<sup>a</sup> Osvaldo Lanzalunga<sup>a</sup>  
and Paola D'Angelo<sup>a,\*</sup>

<sup>a</sup> Dipartimento di Chimica, Università di Roma "La Sapienza",  
P.le A. Moro 5, 00185 Roma, Italy.

, <sup>b</sup> Dipartimento di Chimica, Università degli Studi di Torino,  
Via P. Giuria 7, 10125 Torino, Italy.

<sup>c</sup> The Smart Materials Research Institute, Southern Federal  
University, 344090 Sladkova 178/24 Rostov-on-Don, Russia.

\* p.dangelo@uniroma1.it, francesco.tavani@uniroma1.it

## 1 Materials

All reagents and solvents were employed at the highest commercial quality and were used without further purification. Peracetic acid (36-40 wt% in acetic acid, stored at 4 °C) was acquired from Sigma Aldrich. Fe<sup>II</sup> bis(trifluoromethanesulfonate) from now on referred to as Fe(OTf)<sub>2</sub> was obtained from Strem Chemicals. The N4Py ligand (N4Py = *N,N*-bis(2-pyridylmethyl)-*N*-bis(2-pyridyl)methylamine) was prepared following a previously reported procedure,<sup>1</sup> and metalated to yield [N4Py·Fe<sup>II</sup>(CH<sub>3</sub>CN)](OTf)<sub>2</sub> according to a literature protocol.<sup>2</sup> Preparation and handling of air sensitive materials were carried out under an inert atmosphere by using either Schlenk

and vacuum line techniques or a glove bag under N<sub>2</sub> atmosphere. The complex was then stored under inert atmosphere.

## 2 Methods

### 2.1 Monitoring of the reactions between [N4Py·Fe<sup>IV</sup>(O)]<sup>2+</sup> and the substrates.

Because a pre-mixing cell was not available in the stopped-flow apparatus the [N4Py·Fe<sup>IV</sup>(O)]<sup>2+</sup> solution was prepared in a vial immediately before the execution of the experiment. 1 mL of a 25 mM stock solution of [N4Py·Fe<sup>II</sup>](OTf)<sub>2</sub> was reacted with a solution prepared from 52 μL of a 36-40% w/w solution of peroxyacetic acid in acetic acid (10 eq.) and 200 μL of CH<sub>3</sub>CN to afford a 19.9 mM solution of [N4Py·Fe<sup>IV</sup>(O)]<sup>2+</sup> which was loaded as is in the first syringe of the stopped-flow apparatus. The relatively fast decomposition of the [N4Py·Fe<sup>IV</sup>(O)]<sup>2+</sup> complex at a 20 mM concentration compared to experimental timescales made it necessary to employ more than a stoichiometric amount of oxidant. A solution of the substrate was loaded in the second syringe. The employed concentrations were equal to 300 mM for diphenylmethane (Ph<sub>2</sub>CH<sub>2</sub>) and to 45 mM for 9,10-dihydroanthracene (DHA). The [N4Py·Fe<sup>IV</sup>(O)]<sup>2+</sup> species and the given substrate were then shot in the stopped-flow apparatus in a 3.5:1.0 volume ratio at room temperature in order to attain the final concentration of 8 mM for the [N4Py·Fe<sup>IV</sup>(O)]<sup>2+</sup> complex and the desired concentration of substrate.

### 2.2 Energy dispersive X-ray absorption and UV-Vis measurements.

Simultaneous EDXAS and UV-Vis spectra were collected at ID24 beamline of the european synchrotron radiation facility ESRF, Grenoble (the ring energy was 6.0 GeV and the current 150-200 mA).<sup>3</sup> The X-ray source consists of two undulators whose gaps were tuned to place the first harmonic at 7100 eV. The beam was focused horizontally to an 8 μm full width at half maximum (FWHM) spot on the sample by the curved Si(111) polychromator crystal in Bragg geometry. In the vertical direction, the beam was focused using a bent Si mirror at a glancing angle of 3 mrad with respect to the direct beam. To minimize sample radiation damage, the vertical spot size

was set at 40  $\mu\text{m}$  FWHM. Spectra were recorded in transmission mode using a FReLoN (fast read out low noise) high frame-rate detector based on charge coupled device (CCD) cameras optically coupled with a scintillator screen. Acquisition time was 600 ms and 3.2 s for each spectrum for the reactions involving DHA and  $\text{Ph}_2\text{CH}_2$ , respectively. Sequences of 50-100 individual spectra were acquired and each sequence was repeated three times, and the data were averaged to obtain a better S/N ratio. The energy calibration was made by measuring the absorption spectrum of a Fe foil and the first inflection point was set at 7111 eV. All measurements were carried out at 25°C. Simultaneous EDXAS and UV-Vis spectra were recorded with a Bio-Logic SFM-400 stopped-flow device equipped with a flow-through quartz capillary cell. The quartz capillary cell had a diameter of 1.3 mm and wall thickness of about 10  $\mu\text{m}$ . The dead time of the stopped-flow device is about 2.0 ms for the flow rate of 8 ml/s and it defines the shortest kinetic time that is accessible for spectroscopy measurements. However, for the measurements reported here, the stopped-flow device was triggered by the EDXAS data acquisition system. Therefore, the overhead corresponding to the movement of the syringe motors needs to be considered and the kinetic time starts to evolve 96 ms after the trigger was sent. Therefore, the first UV-Vis spectrum is recorded at the beginning of the reaction ( $t=0$  ms) whereas the first EDXAS spectrum is recorded 24 ms after the reaction starts. From this time on EDXAS and UV-Vis data collection is synchronized.

### 2.3 EDXAS data treatment

The stopped-flow apparatus used to carry out the reaction requires a quartz capillary cell that worsens the EDXAS spectra due to scattering by quartz. For each measurement the EDXAS spectrum of the cell containing pure acetonitrile was collected after the sample spectrum, using the same statistic. The cell spectrum was subtracted from the sample spectrum to gain a better S/N ratio, a higher resolution for the structural oscillations and a more defined Fe K-edge position. The spectra were then subjected to a smoothing procedure using the Savitzky-Golay smoothing filter.<sup>4,5</sup>

The time evolution of the EDXAS reaction spectra is shown in Figure S1 as a two-dimensional plot, where a constant energy cut (dotted line, white) starting from the absorbance maximum of the first experimental spectrum (for both chemical processes) is drawn, together with the evolution of all the spectral maxima (blue, solid line).

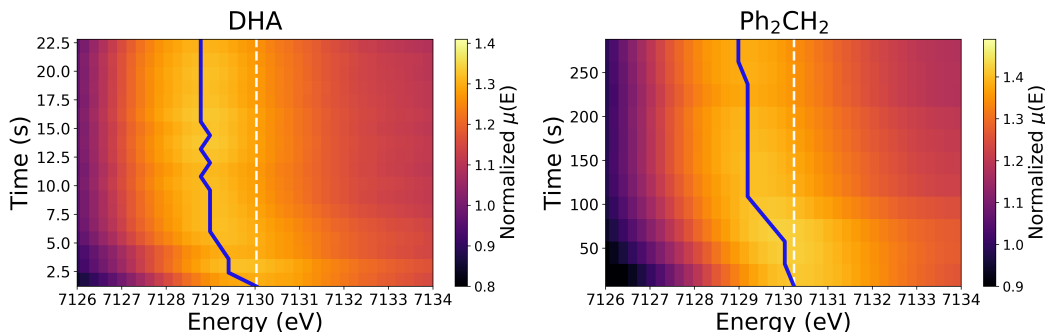


Figure S1: Time evolution of the Fe K-edge EDXAS spectra of the oxidations of DHA (a) and  $\text{Ph}_2\text{CH}_2$  (b) by  $[\text{N4Py}\cdot\text{Fe}^{\text{IV}}(\text{O})]^{2+}$  in  $\text{CH}_3\text{CN}$  at  $25^\circ\text{C}$ . A constant energy cut (white dashed line) is drawn from the absorbance maxima of the first EDXAS spectra. The shift of the time-resolved spectra towards lower energies as the reactions proceed due to the  $\text{Fe}^{\text{IV}}$  reduction (blue full line) is qualitatively evidenced by the deviation of the EDXAS maxima from the dotted line.

## 2.4 Quantification of $\text{Fe}^{\text{II}}$ and $\text{Fe}^{\text{III}}$ in the reaction mixtures

Quantification of  $\text{Fe}^{\text{II}}$  and  $\text{Fe}^{\text{III}}$  in the reaction mixtures was performed adapting a procedure reported by Nam *et al.*<sup>2</sup> Upon completion of the reaction between  $[\text{N4Py}\cdot\text{Fe}^{\text{IV}}(\text{O})]^{2+}$  and the given substrate in the conditions reported above (i.e. when the absorbance due to the  $[\text{N4Py}\cdot\text{Fe}^{\text{II}}(\text{CH}_3\text{CN})]^{2+}$  and  $[\text{N4Py}\cdot\text{Fe}^{\text{IV}}(\text{O})]^{2+}$  species had reached its equilibrium value as determined by 3 subsequent spectra with an interval of 60 s), the mixture was diluted to obtain a final total Fe concentration of 1.6 mM. The resulting solution was placed in a 1 mm quartz cuvette and  $[\text{N4Py}\cdot\text{Fe}^{\text{II}}(\text{CH}_3\text{CN})]^{2+}$  was quantified measuring the absorbance at  $\lambda = 450\text{ nm}$  ( $\epsilon = 6700\text{ M}^{-1}\times\text{cm}^{-1}$ ). 1 mol eq. ferrocene (Fc) from a 0.12M  $\text{CH}_3\text{CN}$  stock solution was added to the cuvette to reduce any  $\text{Fe}^{\text{III}}$  present in the reaction mixture to  $\text{Fe}^{\text{II}}$ . Further additions of Fc were carried out to verify that no increase of the absorbance at  $\lambda = 450\text{ nm}$  occurred. 40 minutes were allowed to pass between each addition.  $\text{Fe}^{\text{III}}$  was then quantified measuring the increase of absorbance at  $\lambda = 450\text{ nm}$  before and after the addition of Fc. In all cases, the final  $\text{Fe}^{\text{II}}$  concentration was checked and compared well with the total Fe concentration. The results for the DHA and  $\text{Ph}_2\text{CH}_2$  reactions are shown

in Figure S2 and Figure S3, respectively.

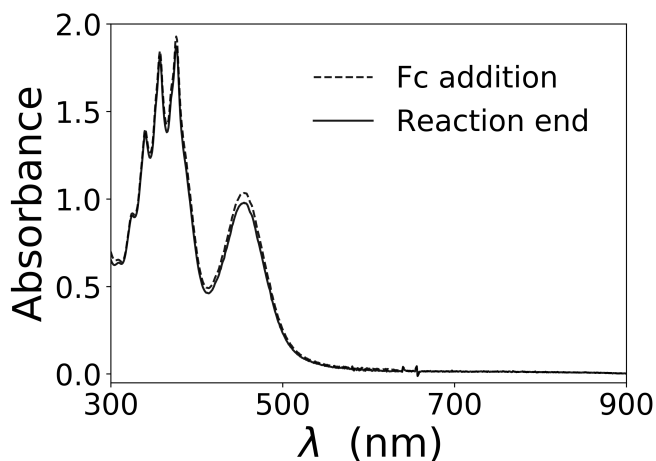


Figure S2: UV-Vis absorption spectra of the reaction mixture of DHA and  $[\text{N4Py}\cdot\text{Fe}^{\text{IV}}(\text{O})]^{2+}$  in the conditions described above at the end of the reaction (full line) and after the addition of ferrocene (dotted line).  $\text{Fe}^{\text{II}}$ : 96%;  $\text{Fe}^{\text{III}}$ : 4%. Initial Fe: 1.6 mM; total Fe: 1.5 mM.

Further, the oxidation of  $\text{Ph}_2\text{CH}_2$  was carried out in the absence of acids, following a protocol reported by Nam for  $\text{Ph}_3\text{CH}$  ( $[\text{N4Py}\cdot\text{Fe}^{\text{IV}}(\text{O})]^{2+}$  2.0 mM generated with PhIO; substrate 100 mM).<sup>2</sup> The reaction was carried out in a 1 mm quartz cuvette and no dilution was necessary: Fc was simply added to the mixture at the end of the reaction. The results are shown in Figure S4.

Finally, the  $\text{Fe}^{\text{II}}$  and  $\text{Fe}^{\text{III}}$  species were quantified in the reaction mixtures at the end of the reaction of  $[\text{N4Py}\cdot\text{Fe}^{\text{IV}}(\text{O})]^{2+}$  (formed by reaction of the  $\text{Fe}^{\text{II}}$  complex with AcOOH 40 mM) with the two substrates added at the same 45 mM concentration. The resulting mixtures were diluted to obtain a final total Fe concentration (2.0 mM). The results are shown in Figure S5.

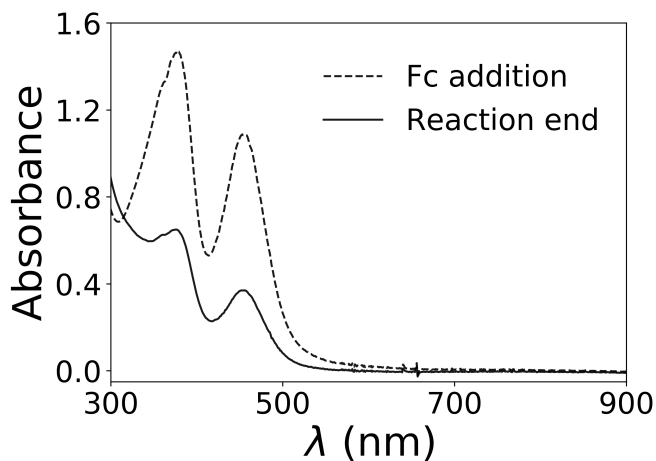


Figure S3: UV-Vis absorption spectra of the reaction mixture of  $\text{Ph}_2\text{CH}_2$  and  $[\text{N4Py}\cdot\text{Fe}^{\text{IV}}(\text{O})]^{2+}$  in the conditions described above at the end of the reaction (full line) and after the addition of ferrocene (dotted line).  $\text{Fe}^{\text{II}}$ : 34%;  $\text{Fe}^{\text{III}}$ : 66%. Initial Fe: 1.6 mM; total Fe: 1.6 mM.

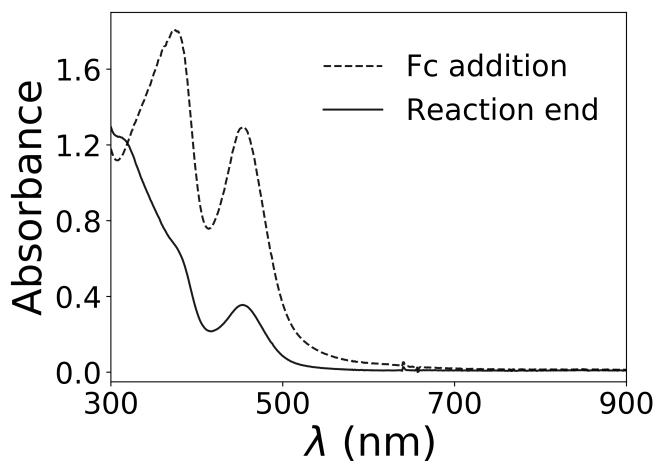


Figure S4: UV-Vis absorption spectra of the reaction mixture relative to the oxidation of  $\text{Ph}_2\text{CH}_2$  by  $[\text{N4Py}\cdot\text{Fe}^{\text{IV}}(\text{O})]^{2+}$ , in the conditions reported by Nam for  $\text{Ph}_3\text{CH}$ ,<sup>2</sup> at the end of the reaction (full line) and after the addition of ferrocene (dotted line).  $\text{Fe}^{\text{II}}$ : 27%;  $\text{Fe}^{\text{III}}$ : 73%. Initial Fe: 2.0 mM; total Fe: 1.9 mM.

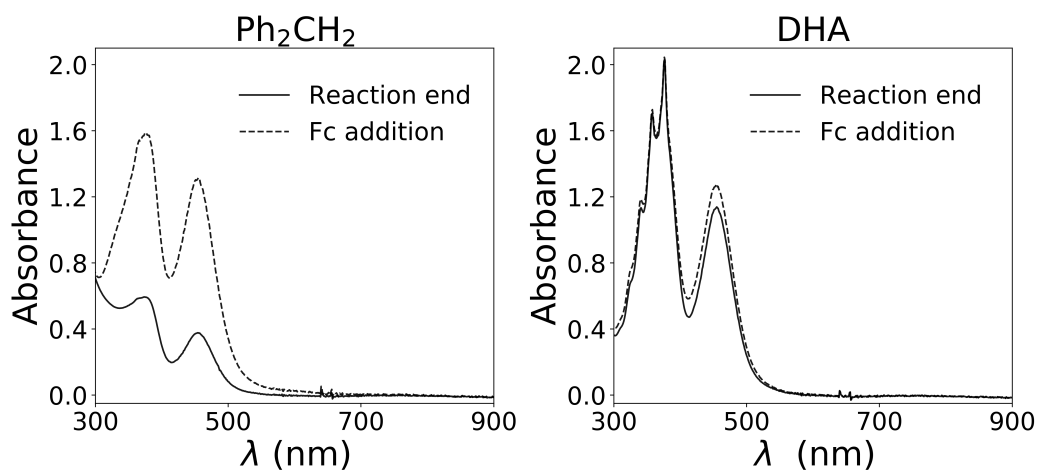


Figure S5: (a) UV-Vis absorption spectra of the reaction mixture of  $\text{Ph}_2\text{CH}_2$  and  $[\text{N4Py}\cdot\text{Fe}^{\text{IV}}(\text{O})]^{2+}$  in the conditions described above at the end of the reaction (full line) and after the addition of ferrocene (dotted line).  $\text{Fe}^{\text{II}}$ : 28%;  $\text{Fe}^{\text{III}}$ : 72%. Initial Fe: 2.0 mM; total Fe: 2.0 mM. (b) UV-Vis absorption spectra of the reaction mixture of DHA and  $[\text{N4Py}\cdot\text{Fe}^{\text{IV}}(\text{O})]^{2+}$  in the conditions described above at the end of the reaction (full line) and after the addition of ferrocene (dotted line).  $\text{Fe}^{\text{II}}$ : 89%;  $\text{Fe}^{\text{III}}$ : 11%. Initial Fe: 2.0 mM; total Fe: 1.9 mM.

## 2.5 UV-Vis reference spectra of $[\text{N4Py}\cdot\text{Fe}^{\text{IV}}(\text{O})]^{2+}$ and $[\text{N4Py}\cdot\text{Fe}^{\text{II}}(\text{CH}_3\text{CN})]^{2+}$

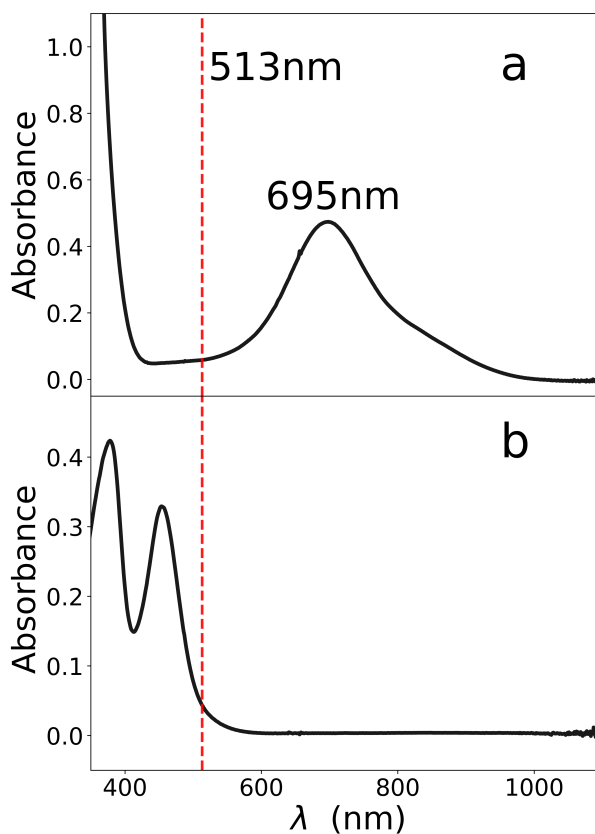


Figure S6: UV-Vis spectra of  $[\text{N4Py}\cdot\text{Fe}^{\text{IV}}(\text{O})]^{2+}$   $1.3 \cdot 10^{-3}$  M (a) and  $[\text{N4Py}\cdot\text{Fe}^{\text{II}}(\text{CH}_3\text{CN})]^{2+}$   $8.5 \cdot 10^{-5}$  M (b) in  $\text{CH}_3\text{CN}$  at  $25^\circ\text{C}$  (optical path: 1 cm). The lowest experimental wavelength (513 nm) and the wavelength corresponding to the absorbance maximum of  $[\text{N4Py}\cdot\text{Fe}^{\text{IV}}(\text{O})]^{2+}$  (695 nm) are indicated.

## 2.6 Determination of the number of principal components through statistical criteria: scree plot and IE factor analysis

The UV-Vis spectroscopic data recorded during the reactions of DHA and Ph<sub>2</sub>CH<sub>2</sub> with [N4Py·Fe<sup>IV</sup>(O)]<sup>2+</sup> were subjected to the scree plot and Imbedded-Error (IE) function analyses to determine the number of pure species present in the reaction mixtures. The UV-Vis data were used in opposition to the EDXAS data for the statistical investigation due to its lower degree of experimental noise. The results of the statistical analyses were the same if applied to the totality of the UV-Vis datasets for the two reactions, or just to the UV-Vis spectra measured with the time resolution of the corresponding EDXAS spectra.

The elements of the diagonal matrix  $\Sigma$  in eq. 1 of the main text are the singular values  $\sigma_{ii}$  extracted by the Singular Value Decomposition (SVD) procedure. One may show that the following expression holds:

$$s_i = \frac{\sigma_{ii}^2}{m - 1} \quad (1)$$

where  $s_i$  are the eigenvalues of the covariance matrix of  $\mathbf{D}$  (evaluated for  $m$  energy steps) and correspond to the variance represented by each principal component (PC),<sup>6,7</sup> while  $n$  is the number of time steps in the time-resolved experiment. Therefore, the components characterized by a large  $\sigma_{ii}$  value will contribute in a significant way to the reconstruction of the dataset, while those with a small  $\sigma_{ii}$  value will be associated to statistical noise. Both the scree plot and the IE-function tests rely on the variance values obtained from eq. 1.

In the scree plot analysis, the singular values relative to each PC are plotted against the number of PCs and the identification of an elbow in the resulting curve marks the distinction between signal and noise related components. Conversely, the IE-function is given by:

$$IE = \sqrt{\frac{h \sum_{i=h+1}^n s_i}{mn(n-h)}} \quad (2)$$

where  $h$  is the number of PCs used for the representation of  $\mathbf{D}$  and  $n$  is the number of time steps in the time-resolved experiment. It can be shown that if the experimental errors are uniformly and randomly distributed for

every spectrum of the dataset  $\mathbf{D}$ , then all secondary PCs possess eigenvalues that are approximately the same.<sup>6,7</sup> This finding leads to the possibility of rewriting eq. 2, for  $h > N$  ( $N$  is the number of PCs necessary to reproduce the experimental data), as:

$$IE = n^{\frac{1}{2}} \cdot k \quad (3)$$

where  $k$  is a constant proportional to the magnitude of the secondary eigenvalues. Therefore, for  $h < N$ , as stated by eq. 2, the IE-function decreases as the number of PCs increases, whereas for  $h > N$  the IE function increases as a function of the number of PCs. This implies that a minimum value is reached at  $h = N$ .

## 2.7 XANES data analysis

Each XANES spectrum extracted from the decomposition of the EDXAS data relative to the oxidation of  $\text{Ph}_2\text{CH}_2$  by  $[\text{N4Py}\cdot\text{Fe}^{IV}(\text{O})]^{2+}$  was assigned to a reaction key species and analyzed using the MXAN code.<sup>8,9</sup> This code is based on the calculation of theoretical spectra with a multiple scattering (MS) approach in the framework of the muffin tin (MT) approximation using a complex optical potential, based on the local density approximation<sup>10-12</sup> of the excited photoelectron self-energy. The MT radii have been calculated according to the Norman criterion. The self-energy is calculated in the framework of the Hedin-Lundqvist (HL) scheme using only the real part of the HL potential while an empirical approach is employed to account for inelastic losses in which the plasmon amplitude,  $A_s$  and the energy onset,  $E_s$  are refined.<sup>13</sup> In all analyses the core hole lifetime  $\Gamma_c$  was kept fixed at 1.25 eV for Fe.

The analysis of the XANES spectrum assigned to the species  $[\text{N4Py}\cdot\text{Fe}^{II}(\text{CH}_3\text{CN})]^{2+}$  was carried out starting from an octahedral coordination model around the Fe atoms based on the crystallographic structure<sup>14</sup> of the same complex. In this structure the Fe photoabsorber is coordinated by four nitrogen atoms belonging to the N4Py backbone ( $\text{N}_{Py}$ ), by one nitrogen atom bound to three carbon atoms ( $\text{N}_{amine}$ ) and by a  $\text{CH}_3\text{CN}$  solvent nitrogen atom ( $\text{N}_{ACN}$ ). The minimization procedure of the Fe(II) species has been carried out by optimizing the four Fe- $\text{N}_{Py}$  distances, the Fe- $\text{N}_{amine}$  and the Fe- $\text{N}_{ACN}$  single distances. The orientation of the  $\text{CH}_3\text{CN}$  molecule was optimized within a preset range of  $\pm 30^\circ$  around the initial structure, whereas the orientation of the rest of the molecule was optimized within  $\pm 1^\circ$ .

The XANES calculations regarding complex  $[\text{N4Py}\cdot\text{Fe}^{IV}(\text{O})]^{2+}$  were based on the previously reported X-ray crystallography molecular structure.<sup>15</sup> In this complex, the central metal cation is coordinated to the four N4Py nitrogen atoms, to the  $\text{N}_{amine}$  nitrogen atom and to an oxygen atom. The minimization procedure was applied by optimizing all the Fe- $\text{N}_{Py}$ , Fe- $\text{N}_{amine}$  and the Fe-O distances independently. The orientation of the oxygen atom and of the rest of the molecule were optimized within a preset range of  $\pm 30^\circ$  and  $\pm 2^\circ$  around the initial structure, respectively. All the mentioned Fe–ligand distances relative to the  $\text{Fe}^{IV}$  and  $\text{Fe}^{II}$  complexes were allowed to vary within  $\pm 0.05$  Å of the crystallographic ones.

The MS analysis of  $[\text{N4Py}\cdot\text{Fe}^{III}(\text{OH})]^{2+}$  has been carried out starting from the crystallographic structure of complex  $[\text{N4Py}\cdot\text{Fe}^{IV}(\text{O})]^{2+}$ . Also in this case, all the Fe- $\text{N}_{Py}$ , Fe- $\text{N}_{amine}$  and the Fe-O distances were independently refined. The orientation of the oxygen atom and of the rest of the molecule were minimized within a preset range of  $\pm 25^\circ$  and  $\pm 3^\circ$  around the initial structure, respectively.

Hydrogen atoms have not been included in all MXAN analyses. For all spectra, the nonstructural parameters have been optimized, namely, the threshold energy,  $E_0$ , the Fermi energy level,  $E_F$ , and the energy and amplitude of the plasmon,  $E_s$  and  $A_s$ . The quality of the fits has been estimated with the residual function,  $R_{sq}$ .<sup>8–10</sup> The best-fit results are shown in Figure S7, while the full list of the associated nonstructural parameters is presented in Table S1.

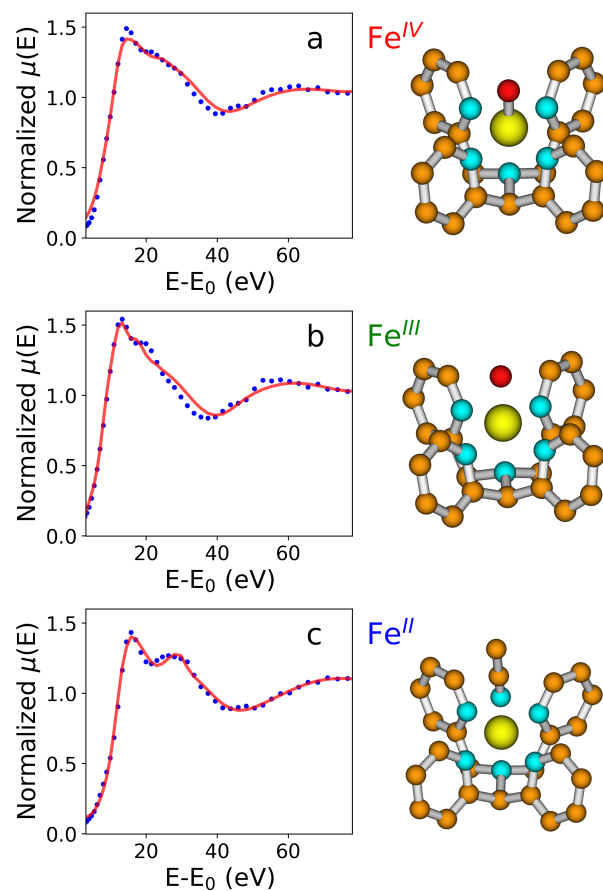


Figure S7: Best-fit results of the analysis of the XANES spectra extracted for the reaction between  $\text{Ph}_2\text{CH}_2$  and  $[\text{N4Py}\cdot\text{Fe}^{\text{IV}}(\text{O})]^{2+}$ . The Fe K-edge XANES spectra (blue, dotted lines) are assigned to complexes  $[\text{N4Py}\cdot\text{Fe}^{\text{IV}}(\text{O})]^{2+}$  (a),  $[\text{N4Py}\cdot\text{Fe}^{\text{III}}(\text{OH})]^{2+}$  (b) and  $[\text{N4Py}\cdot\text{Fe}^{\text{II}}(\text{CH}_3\text{CN})]^{2+}$  (c) and compared to the theoretical curves (red, full lines) calculated with optimized geometrical models. The associated molecular clusters are also depicted, where iron, nitrogen, carbon and oxygen atoms are in yellow, cyan, orange and red, respectively.

	$E_0(eV)$	$E_F(eV)$	$E_s(eV)$	$A_s$	$R_{sq}$
<b>Fe<sup>IV</sup></b>	-4.1	2.8	25.5	9.4	1.6
<b>Fe<sup>III</sup></b>	-3.8	2.7	23.1	7.5	1.9
<b>Fe<sup>II</sup></b>	-6.9	1.8	31.3	10.6	1.3

Table S1: Nonstructural parameters obtained from the MXAN analysis of the Fe K-edge XANES spectra of the  $[\text{N4Py}\cdot\text{Fe}^{IV}(\text{O})]^{2+}$  ( $\text{Fe}^{IV}$ ),  $[\text{N4Py}\cdot\text{Fe}^{III}(\text{OH})]^{2+}$  ( $\text{Fe}^{III}$ ) and  $[\text{N4Py}\cdot\text{Fe}^{II}(\text{CH}_3\text{CN})]^{2+}$  ( $\text{Fe}^{II}$ ) complexes.  $E_0$  is the threshold energy,  $E_F$  is the Fermi energy level,  $E_s$  and  $A_s$  are the energy and amplitude of the plasmon,  $R_{sq}$  is the residual function.

## References

- [1] M. Lubben, A. Meetsma, E. C. Wilkinson, B. Feringa and L. Que Jr., *Angew. Chem. Int. Ed.*, 1995, **34**, 1512–1514.
- [2] K.-B. Cho, X. Wu, Y.-M. Lee, Y. H. Kwon, S. Shaik and W. Nam, *J. Am. Chem. Soc.*, 2012, **134**, 20222–20225.
- [3] S. Pascarelli, O. Mathon, T. Mairs, I. Kantor, G. Agostini, C. Strohm, S. Pasternak, F. Perrin, G. Berruyer, P. Chappelet, C. Clavel and M. C. Dominguez, *J. Synchr. Rad.*, 2016, **23**, 353–368.
- [4] W. H. Press, S. a. Teukolsky, W. T. Vetterling and B. P. Flannery, *Numerical Recipes in Fortran 77: the Art of Scientific Computing. Second Edition*, 1996, vol. 1.
- [5] P. A. Gorry, *Anal. Chem.*, 1990, **62**, 570–573.
- [6] I. Markovsky, *Automatica*, 2008, **44**, 891–909.
- [7] A. Martini, S. Guda, A. Guda, G. Smolentsev, A. Algasov, O. Usoltsev, M. Soldatov, A. Bugaev, Y. Rusalev, C. Lamberti and A. Soldatov, *Comput. Phys. Comm.*, 2019, 107064.
- [8] M. Benfatto and S. Della Longa, *J. Synchr. Rad.*, 2001, **8**, 1087–1094.
- [9] M. Benfatto, S. Della Longa and C. R. Natoli, *J. Synchr. Rad.*, 2003, **10**, 51–57.
- [10] P. D’Angelo, A. Zitolo, G. Aquilanti and V. Migliorati, *J. Phys. Chem. B*, 2013, **117**, 12516–12524.
- [11] E. Burattini, P. D’Angelo, A. Di Cicco, A. Filipponi and N. V. Pavel, *J. Phys. Chem.*, 1993, **97**, 5486–5494.
- [12] K. Hayakawa, K. Hatada, P. D’Angelo, S. Della Longa, C. Natoli and M. Benfatto, *J. Am. Chem. Soc.*, 2005, **126**, 15618–23.
- [13] P. D’Angelo and V. Migliorati, *J. Phys. Chem. B*, 2015, **119**, 4061–4067.

- [14] G. Roelfes, M. Lubben, K. Chen, R. Y. N. Ho, A. Meetsma, S. Genseberger, R. M. Hermant, R. Hage, S. K. Mandal, V. G. Young, Y. Zang, H. Kooijman, A. L. Spek, L. Que and B. L. Feringa, *Inorg. Chem.*, 1999, **38**, 1929–1936.
- [15] E. J. Klinker, J. Kaizer, W. W. Brennessel, N. L. Woodrum, C. J. Cramer and L. Que Jr., *Angew. Chem. Int. Ed.*, 2005, **44**, 3690–3694.